International Journal of Greenhouse Gas Control 5 (2011) 986–994

Contents lists available at ScienceDirect

International Journal of Greenhouse Gas Control

journal homepage: www.elsevier.com/locate/ijggc

Numerical simulation of convective stability of the short-term storage of CO_2 in saline aquifers

Yang Duoxing[a,b,*], Zeng Rongshu[b], Zhang Deliang[c]

[a] Institute of Geology and Geophysics, CAS, Beijing 100029, China
[b] Institute of Crustal Dynamics, CEA, Beijing 100085, China
[c] LHD Lab Institute of Mechanics, CAS, Beijing 100190, China

ARTICLE INFO

Article history:
Received 14 April 2010
Received in revised form 31 October 2010
Accepted 6 November 2010
Available online 3 December 2010

Keywords:
Multiphase flow
CO_2 storage
CE/SE method
Hybrid particle level set method

ABSTRACT

In this paper, inertial effects, mass interface and mass transfer mechanism are taken into account. By applying an updated space and time conservation element and solution element (CE/SE) method and hybrid particle level-set method, the stability simulation of the density-driven convection in deep saline aquifers is presented for short-term storage of CO_2. The mass transfer equations coupled with two phase fluid flow equations are solved numerically to investigate effects of CO_2 dissolution into brine on migration. Results show that Taylor instability phenomenon has been observed in CO_2 storage in saline aquifers for short time scales, which contributes to the further dissolution of CO_2 in saline aquifers. Density-driven convection dominates hydrodynamic trapping, while dissolution process of CO_2 also has a great influence on CO_2 sequestration.

1. Introduction

Both China and the world are facing the pressure and challenge of climate change. CCS (CO_2 capture and storage) is one of the prior solutions to reduce CO_2 emission under the current energy structure. The most promising way of achieving CO_2 reduction is to inject of CO_2 in deep saline aquifers (Bachu et al., 1994; Hitchon et al., 1999; John, 2004). The saline aquifers have a large potential for CO_2 sequestration in geological medium (Soong et al., 2004). There are three mechanisms for CO_2 storage in saline aquifers (Hitchon et al., 1999). First, CO_2 can be trapped as supercritical fluid or a gas in a formation, referred as hydrodynamic trapping. Second, CO_2 can dissolve into the brine groundwater, called solubility trapping. The third mechanism is mineral trapping, where CO_2 can react directly or indirectly with minerals in the geological formation, resulting in the precipitation of secondary carbonates. Of the three mechanisms, hydrodynamic trapping dominates CO_2 migration and build-up in saline aquifers for short-time scales (Bachu, 2000). Density-driven convection due to the larger density of brine than that of CO_2 mainly contributes to the hydrodynamic trapping process, and plays an important role in determining the ultimate fate of CO_2 in saline aquifers (Kenta et al., 2008). The density-driven convection in porous media can be analogous to the temperature-driven Rayleigh–Benard convection (Lapwood, 1948). The onset of transient convective instability in isotropic porous media has been investigated by many researchers through linear (Caltagirone, 1980) and non-linear (Straughan and Walker, 1996) stability analyses. The transient linear stability analysis in an anisotropic porous medium was performed by Ennis and Paterson (2003). Recently, Xu et al. (2006) studied the density-driven convection due to the larger density of CO_2 saturated brine (approximately 10 kg/m^3 denser) than that of the unsaturated brine. The effects of both vertical and horizontal permeability variations on the stability criteria were considered. The stability criteria and critical time for the appearance of convective phenomena were studied with both linear and global stability analyses for long-term storage of carbon dioxide (CO_2), with anisotropic permeability. However, whether such a disturbance leads to continuous convective mixing may be addressed by resorting to high-resolution two phase flow simulations.

Investigation found that when the supercritical CO_2 is injected into deep saline aquifers above the critical point of CO_2, because the density of supercritical CO_2 ($ScCO_2$) is lower than that of brine, the $ScCO_2$ will migrate upwards after injection. In the density-driven convection process, the heavier brine will migrate downward and be replaced by $ScCO_2$. The convective mixing will greatly accelerate the solubility trapping. The speed of convection is partially orders of magnitude faster than that of pure diffusion (Xu et al., 2006). To our best knowledge, a novel contribution on the instability of $ScCO_2$–water interface (as shown in Fig. 1) during upward migration has not been investigated, and it is obviously different from the

* Corresponding author at: Institute of Geology and Geophysics, Chinese Academy of Sciences, No. 1, Beitucheng West Rd, Chaoyang District, Beijing 100029, China. Tel.: +86 10 82998645; fax: +86 10 82998645.
E-mail address: yangdx@mail.iggcas.ac.cn (D. Yang).

1750-5836/$ – see front matter © 2010 Elsevier Ltd. All rights reserved.
doi:10.1016/j.ijggc.2010.11.004

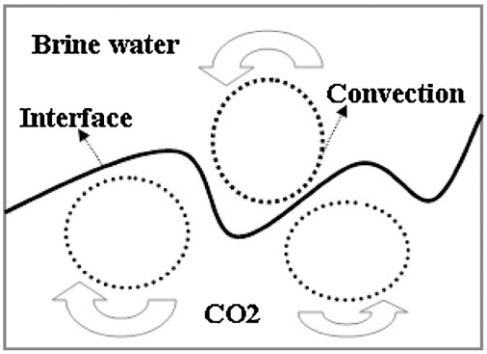

Fig. 1. Schematic map of phase interface and its instability in saline aquifers.

density-driven convection of CO_2 saturated brine as investigated in the previous studies.

The instability of CO_2–water interface in deep saline aquifers is highly nonlinear phenomena and hardly described by analytical solutions. Hence numerical methods have to be proposed and applied. However, two primary challenges are still confronted in the numerical methods, including the numerical scheme for the governing equations and the special treatments for the fluid or phase interfaces. The governing equations for the multiphase flows in CO_2 storage can be traditionally formulated in two ways known as Lagrangian and Eulerian method. The main limitation of the Lagrangian approach is that the results are inaccurate with using the finite difference approximation when the grid cells are distorted significantly. The Eulerian approach is difficult to identify the phase interfaces accurately at each time step. Therefore, a high-accuracy fluid or phase interface tracing algorithm must be adopted for the Eulerian approach. The CE/SE method (the space–time conservation element and solution element method) originally proposed by Chang (1995) is a novel high-resolution CFD method for hyperbolic conservation laws. The hybrid particle level set method (HPLS) was developed by Enright et al. (2002), which is a robust technique to capture phase interfaces.

In this paper, the study focus is placed on the physical conservation laws in order to capture multiphase fluid physics process, phase interfaces (CO_2/brine water) and stability of phase interfaces more efficiently and realistically. The higher-order CE/SE (space and time conservation element and solution element) method is applied to simulate key aspects of hydrodynamic trapping and solubility trapping. The hybrid particle level-set (HPLS) method, which can accurately capture phase interfaces between CO_2 and brine, is also used. The experimental results of water and kerosene interaction in T-shaped tube and the dam break problem are utilized to evaluate and validate the proposed method. The onset of transient convective instability of CO_2 storage in isotropic porous saline aquifers is numerically simulated. Then CO_2 dissolution into saline aquifer is also investigated. This paper presents a phase interface mechanism for the stability simulation of the density-driven convection, which could be useful for fundamental studies on two-phase CO_2–water flow dynamics with possible applications to CO_2 storage in deep saline aquifers.

2. Numerical method

2.1. Governing equations

We assume that (1) the supercritical CO_2 and brine water are immiscible, and the saline aquifer is the isotropic and homogeneous porous media. Thermal equilibrium is also assumed; (2) the two fluids are viscous, Newtonian and incompressible; (3) the flow is isothermal, the interface tension is taken as constant and there is no interfacial resistance to mass transfer; and (4) CO_2 dissolution is assumed to have no effect on the physical properties of the system.

Based on the most robust derivation of the volume-averaged Navier–Stokes equations performed by Whitaker (1996) and Liu et al. (2007), a set of governing equations for mass and momentum is obtained as follows:

Continuity equation:

$$\frac{\partial u_i}{\partial x_i} = 0 \tag{1}$$

Momentum equation:

$$\frac{\partial u_i}{\partial t} + \frac{\partial}{\partial x_j}\left(\frac{1}{\varphi}u_i u_j\right) = -\frac{\varphi}{\rho}\frac{\partial P}{\partial x_i} + \frac{1}{\rho}\frac{\partial}{\partial x_j}\left(\mu\left(\frac{\partial u_i}{\partial x_j} + \frac{\partial u_j}{\partial x_i}\right)\right) - \frac{\varphi\mu}{\rho K}u_i - \frac{\varphi F_b}{\sqrt{K}}u_i\sqrt{u_i^2 + u_j^2} - \frac{\varphi}{\rho}\vec{F}_{SV} - \varphi g_i \tag{2}$$

where u_i, u_j and P are the volume-averaged velocities and pressure, respectively. K is called the permeability tensor, φ is porosity, and t presents time. There exist two viscous terms. The first is the Laplacian term (the second term on the right) analogous to that in the Navier–Stokes equation and the second is the usual Darcy term (the third term on the right). The Forchheimer term (the fourth term on the right) in Eq. (2) represents a volume-averaged drag term due to inertial effects. The five term on the right is referred as the surface tension force. By employing a CSF (continuum surface force) model (Brackbill et al., 1992) of the surface tension force for the level set approach (Osher and Sethian, 1988), the surface tension is reformulated as a volume force,

$$\vec{F}_{SV} = k(\phi)\delta_\alpha(\phi)\nabla\phi \tag{3}$$

where ϕ is a smooth level set function, which is positive outside the interface, negative inside the interface and zero at the interface. δ is a surface tension delta function and k is the interface front curvature. In a two-dimensional coordinate system, mass and momentum conservation (Yang et al., 2010) with the level set approach incorporated are written in terms of dimensionless variables, with dimensionless groups of the Reynolds, Froude, Weber numbers, Darcy number and inertial factor as $\mathrm{Re} = \rho_o LU/\mu_o$, $\mathrm{Fr} = U^2/gL$, $\mathrm{We} = \rho_o LU^2/\sigma_o$, $\mathrm{Da} = K/L^2$, and $F_b = 1.75/\sqrt{150\phi^3}$, respectively. $\bar{\rho}$ and $\bar{\mu}$ are the dimensionless ratios of the viscosity and density. φ is the porosity. For further detailed information about the non-dimensional equations, readers should refer to the lecture (Yang et al., 2010). For simplicity, hereafter we denote λ_ρ and λ_μ as $\bar{\rho}$ and $\bar{\mu}$, respectively. To prevent numerical instability, it is necessary to smooth the values of the density ρ_ε and viscosity μ_ε as:

$$\begin{aligned}\rho_\varepsilon(\phi) &= \lambda_\rho + (1-\lambda_\rho)H_\varepsilon(\phi)\\ \mu_\varepsilon(\phi) &= \lambda_\mu + (1-\lambda_\mu)H_\varepsilon(\phi)\end{aligned} \tag{4}$$

where the Heaviside function (Enright et al., 2002) $H_\varepsilon(\phi)$ is formulated as followings:

$$H_e(\phi) = \begin{cases} 0 & \phi < -\varepsilon \\ \frac{1}{2}\left(1 + \frac{\phi}{\varepsilon} + \frac{1}{\pi}\sin\left(\frac{\pi\phi}{\varepsilon}\right)\right) & |\phi| \le \varepsilon \\ 1 & \phi > \varepsilon \end{cases} \tag{5}$$

2.2. Mass transport equation

The equation of mass transport is formulated as followings (Yang and Mao, 2005)

$$\frac{\partial C_i}{\partial t} + \frac{\partial (C_i u_j)}{\partial x_j} = \frac{\partial}{\partial x_j}\left(D_i\frac{\partial C_i}{\partial x_j}\right) \tag{6-1}$$

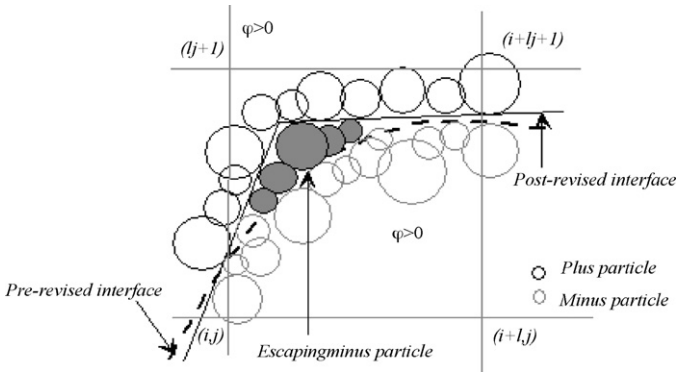

Fig. 2. Schematic map of hybrid particle level-set method (HPLS).

where i indicates the group, D_i is the diffusion coefficient, and C_i is the concentration for each phases. The quantitative simulation of interphase mass transfer is turned out to be especially challenging, because different diffusivities in two liquid phases result in the discontinuity of concentration gradient, and the distribution coefficient of a solute not equal to unity leads to the solute concentration discontinuous across the interface. We refer reader to Yang et al. (2006) for detail description to overcome this challenge.

2.3. Interface treatment method: hybrid particle level-set method

Based on volume-averaged concept and ordinary level-set method (Osher and Sethian, 1988), the following equation will evolve the zero level set function in porous media (Yang et al., 2010; Yang and Zhang, 2010):

$$\varphi\frac{\partial\phi}{\partial t}+u_i\frac{\partial\phi}{\partial x_i}=0 \tag{6-2}$$

The above level set equation is solved using a five-order WENO discretization and Runge–Kutta method (Jiang and Peng, 2000). Sussman et al. (1994) presented a reinitialization equation insure that values for level set function will not be greatly distorted. The reinitialization equation can be reformulated as:

$$\begin{aligned}&\phi_\tau+w\cdot\nabla\phi=\mathrm{sign}_\varepsilon(\phi_o)\\&\phi(\vec{x},0)=\phi_o(\vec{x})\end{aligned} \tag{7}$$

where $w=\mathrm{sign}_\varepsilon(\phi_o)\nabla\phi/|\nabla\phi|$, $|\nabla\phi|=\sqrt{\phi_x^2+\phi_y^2+\phi_z^2}$, and $\mathrm{sign}_\varepsilon(\phi_o)=2(H_\varepsilon(\phi_o)-1/2)$ the sign function. The numerical discretization of the reinitialization equation of the level set function will not preserve the total mass conservation. To overcome this difficulty, the hybrid particle level set (HPLS) method (Enright, 2002) can be presented to conduct the solution of the reinitialization equation. Particle level set method is a coupling method of Lagrangian method and Eulerian method, which merges the best aspects of Eulerian front capturing schemes and Lagrangian front-tracking methods for improved mass conservation in a fluid flow. Massless marker particles were inserted to correct mass loss in level set function using the characteristic information of the escaped massless marker (as shown in Fig. 2). The particle level set method maintains the nice geometric properties of level set method, and performs favorably in the conservation of mass and for interface resolution. The particle Lagrangian function is written as:

$$\frac{d\bar{r}_p}{dt}=\bar{V}(\bar{r}_p) \tag{8}$$

where $\bar{r}_p$ is the location of the particle, and $\bar{V}$ is the particle velocity. The third-order Runge–Kutta scheme is used to solve Eq. (8).

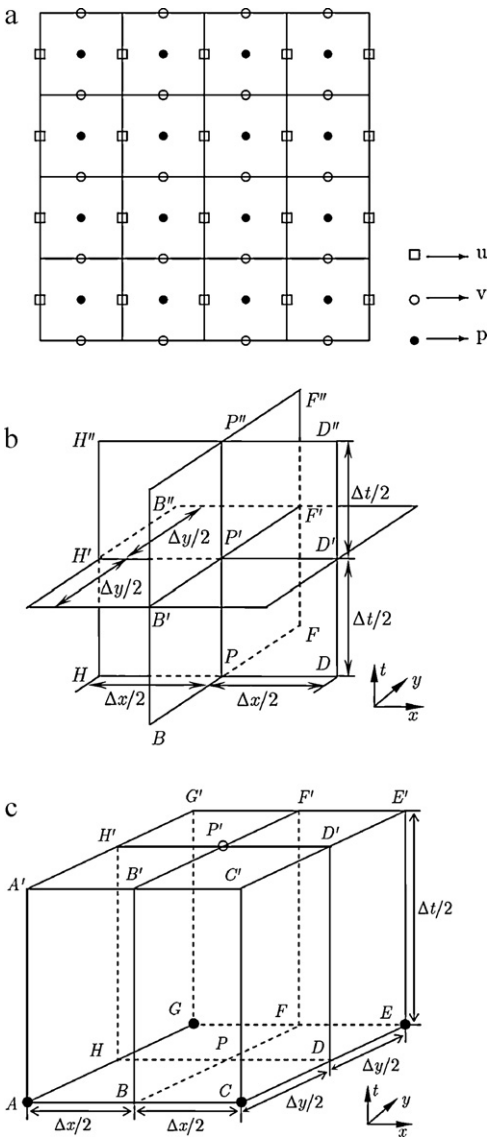

Fig. 3. Mesh construction of the updated CE/SE method: (a) mesh points projection on xy plane, (b) conservation element CE(P'), and (c) solution element SE(P').

For further detailed information about the HPLS method, readers should refer to the literature (Enright et al., 2002).

2.4. CE/SE method

The CE/SE method (the space–time conservation element and solution element method) originally proposed by Chang (1995) is a novel high-resolution CFD method for hyperbolic conservation laws. In this paper, an updated space–time conservation element and solution element (CE/SE) scheme is proposed. The SEs (solution elements) and CEs (conservation elements) are demonstrated in Fig. 3. The governing Eqs. (1) and (2) can be rewritten as the Euler equation (Wang et al., 2009; Yang et al., 2009):

$$\frac{\partial\mathbf{Q}}{\partial t}+\frac{\partial\mathbf{E}(\mathbf{Q})}{\partial x}+\frac{\partial\mathbf{F}(\mathbf{Q})}{\partial y}=S(\mathbf{Q}) \tag{9}$$

where $\mathbf{Q}$, $\mathbf{E}$, $\mathbf{F}$, and $\mathbf{S}$ are vectors of the primary variable, fluxes in the (x, y) directions and the source term, respectively. Wang et al. (2009) and Yang et al. (2009) proposed an improved CE/SE method with the first order accuracy by adopting general hexahedrons mesh to construct CEs and SEs,

which is different from that of the Chang's (1995) original CE/SE method.

Here, we deduce the two-dimensional CE/SE scheme with the second-order accuracy for flows in porous medium. Let j, k, and n denote a set of space–time mesh points, where $n = 0, \pm(1/2), \pm 1, \pm(3/2), \ldots$ for time, $j = 0, \pm(1/2), \pm 1, \pm(3/2), \ldots$ for x, and $k = 0, \pm(1/2), \pm 1, \pm(3/2), \ldots$ for y. A SE is defined as the vicinity of a mesh point and the whole space–time region is divided into non-overlapping CEs. Assume that the physical variables in every SE are approximated by the Taylor's expansions at the mesh point associated with the SE, and the conservation Eq. (4) is satisfied in every CE. Let $x_1 = x$, $x_2 = y$, and $x_3 = t$, be considered as the coordinates of a Euclidean space E_3. By means of the Gauss' divergence theorem, Eq. (9) is rewritten in form of:

$$\oint_{S(v)} \mathbf{H}_m \cdot d\mathbf{s} = \int S_m dV \tag{10}$$

where $\mathbf{H}_m = (E_m, F_m, Q_m)$ is the space–time flux vector. Here, Q_m, E_m and F_m are the components of vector $\mathbf{Q}$, $\mathbf{E}$ and $\mathbf{F}$, respectively. S_m is the components of the source term vector. $S(V)$ is the boundary of an arbitrary space–time region V in E_3, $d\mathbf{s} = d\sigma \cdot \mathbf{n}$ with $d\sigma$ and $\mathbf{n}$, respectively, being the area and the outward unit normal of a surface element on $S(V)$. Fig. 3(a) shows the projection of mesh points on the $x-y$ plane, in which the interval between the mesh points ● and ○ is $\Delta t/2$ in the time coordinate or 1/2 in the mesh number n. For any point $P'(j, k, n)$ on which the variables are solved, define the solution element SE(P') constituted by the three vertical planes intersecting at $P'(j, k, n)$ and their neighborhood space as demonstrated in Fig. 3(b). Suppose that Q_m, E_m and F_m at point (t, x, y) in SE (P') are approximated by the second-order Taylor expansions at $P'(j, k, n)$, i.e.,

$$\begin{aligned}
Q_m(dx, dy, dt)_{P'} &= (Q_m)_{P'} + (Q_{mx})_{P'}dx + (Q_{my})_{P'}dy + (Q_{mt})_{P'}dt \\
&+ \frac{1}{2}(Q_{mxx})_{P'}(dx)^2 + \frac{1}{2}(Q_{myy})_{P'}(dy)^2 + \frac{1}{2}(Q_{mtt})_{P'}(dt)^2 \\
&+ (Q_{mxt})_{P'}(dx \cdot dt) + (Q_{myt})_{P'}(dy \cdot dt) + (Q_{mxy})_{P'}(dx \cdot dy) \\
E_m(dx, dy, dt)_{P'} &= (E_m)_{P'} + (E_{mx})_{P'}dx + (E_{my})_{P'}dy + (E_{mt})_{P'}dt \\
&+ \frac{1}{2}(E_{mxx})_{P'}(dx)^2 + \frac{1}{2}(E_{myy})_{P'}(dy)^2 + \frac{1}{2}(E_{mtt})_{P'}(dt)^2 \\
&+ (E_{mxt})_{P'}(dx \cdot dt) + (E_{myt})_{P'}(dy \cdot dt) + (E_{mxy})_{P'}(dx \cdot dy) \\
F_m(dx, dy, dt)_{P'} &= (F_m)_{P'} + (F_{mx})_{P'}dx + (F_{my})_{P'}dy + (F_{mt})_{P'}dt \\
&+ \frac{1}{2}(F_{mxx})_{P'}(dx)^2 + \frac{1}{2}(F_{myy})_{P'}(dy)^2 + \frac{1}{2}(F_{mtt})_{P'}(dt)^2 \\
&+ (F_{mxt})_{P'}(dx \cdot dt) + (F_{myt})_{P'}(dy \cdot dt) + (F_{mxy})_{P'}(dx \cdot dy)
\end{aligned} \tag{11}$$

here $dx = x - x_{P'}$, $dy = y - y_{P'}$ and $dt = t - t_{P'}$ where $x_{P'}$, $y_{P'}$ and $t_{P'}$ are the position coordinates of point P'. Substituting Eq. (11) into Eq. (9) gives

$$\begin{aligned}
(Q_{mt})_{P'} &= -(E_{mx})_{P'} - (F_{my})_{P'} + (S_m)_{P'} \\
(Q_{mxt})_{P'} &= -(E_{mxx})_{P'} - (F_{mxy})_{P'} + (S_{mx})_{P'} \\
(Q_{myt})_{P'} &= -(E_{mxy})_{P'} - (F_{myy})_{P'} + (S_{my})_{P'} \\
(Q_{mtt})_{P'} &= -(E_{mxt})_{P'} - (F_{myt})_{P'} + (S_{mt})_{P'}
\end{aligned} \tag{12}$$

The above equations imply that the variables required in computation are $(Q_m)_{P'}$, $(Q_{mx})_{P'}$ and $(Q_{my})_{P'}$, because S_m, E_m, and F_m are the function of Q_m. Define the conservation element CE(P') as illustrated in Fig. 3(c). It can be seen that CE(P') is related to not only SE(P') but also to the SEs of SE(A), SE(C), SE(E) and SE(G). Note that the values of physical variables on mesh points A, C, E and G are given. Assume that the integral conservation laws are satisfied for every CE. Integrating Eq. (10) on the surfaces of CE(P') with the aid of Eq. (11), we find:

$$\begin{aligned}
&(Q_m)_{P'} + \frac{1}{24}\frac{\Delta x}{\Delta y}(Q_{mxx})_{P'} + \frac{1}{24}\frac{\Delta y}{\Delta x}(Q_{myy})_{P'} - \frac{\Delta t}{4}(S_m)_{P'} \\
&= \frac{1}{4}\left(\bar{Q} + \frac{\Delta t}{\Delta x}\bar{E} + \frac{\Delta t}{\Delta y}\bar{F} + \frac{\Delta t}{4}\bar{S}\right)
\end{aligned} \tag{13}$$

where

$$\begin{aligned}
\bar{Q} &= Q_m\left(A, \frac{\Delta x}{4}, \frac{\Delta y}{4}, 0\right) + Q_m\left(C, -\frac{\Delta x}{4}, \frac{\Delta y}{4}, 0\right) \\
&\quad + Q_m\left(E, -\frac{\Delta x}{4}, -\frac{\Delta y}{4}, 0\right) + Q_m\left(G, \frac{\Delta x}{4}, -\frac{\Delta y}{4}, 0\right) \\
\bar{E} &= E_m\left(A, 0, \frac{\Delta y}{4}, \frac{\Delta t}{4}\right) - E_m\left(C, 0, \frac{\Delta y}{4}, \frac{\Delta t}{4}\right) \\
&\quad - E_m\left(E, 0, -\frac{\Delta y}{4}, \frac{\Delta t}{4}\right) + E_m\left(G, 0, -\frac{\Delta y}{4}, \frac{\Delta t}{4}\right) \\
\bar{F} &= F_m\left(A, \frac{\Delta x}{4}, 0, \frac{\Delta t}{4}\right) + F_m\left(C, -\frac{\Delta x}{4}, 0, \frac{\Delta t}{4}\right) \\
&\quad - F_m\left(E, -\frac{\Delta x}{4}, 0, \frac{\Delta t}{4}\right) - F_m\left(G, \frac{\Delta x}{4}, 0, \frac{\Delta t}{4}\right) \\
\bar{S} &= S_m(A) + S_m(C) + S_m(E) + S_m(G)
\end{aligned} \tag{14}$$

Using the continuity conditions at points A', C', E' and G', the derivatives of Q_m with respect to x and y are obtained as follows:

$$\begin{aligned}
(Q_x)_{P'} &= W[(Q_x)^-_{P'}, (Q_x)^+_{P'}, \alpha] \\
(Q_y)_{P'} &= W[(Q_y)^-_{P'}, (Q_y)^+_{P'}, \alpha]
\end{aligned}$$

$$\begin{aligned}
(Q_{mxx})_{P'} &= \frac{1}{\Delta x}[(Q_{mx})_{D'} - (Q_{mx})_{H'}] \\
(Q_{myy})_{P'} &= \frac{1}{\Delta y}[(Q_{my})_{F'} - (Q_{my})_{B'}] \\
(Q_{mxy})_{P'} &= \frac{1}{2}[(\widehat{Q}_{mxy})_{P'} + (\widehat{Q}_{myx})_{P'}]
\end{aligned} \tag{15}$$

where

$$\begin{aligned}
(Q_{mx})_{D'} &= \frac{Q_{mx}(C, 0, 0, \Delta t/2) + Q_{mx}(E, 0, 0, \Delta t/2)}{2} \\
(Q_{mx})_{H'} &= \frac{Q_{mx}(G, 0, 0, \Delta t/2) + Q_{mx}(A, 0, 0, \Delta t/2)}{2} \\
(Q_{my})_{F'} &= \frac{Q_{my}(E, 0, 0, \Delta t/2) + Q_{my}(G, 0, 0, \Delta t/2)}{2} \\
(Q_{my})_{B'} &= \frac{Q_{my}(A, 0, 0, \Delta t/2) + Q_{my}(C, 0, 0, \Delta t/2)}{2} \\
(\widehat{Q}_{mxy})_{P'} &= \frac{\begin{array}{l}Q_{mx}(C, 0, 0, \Delta t/2) - Q_{mx}(A, 0, 0, \Delta t/2) \\ + Q_{mx}(E, 0, 0, \Delta t/2) - Q_{mx}(G, 0, 0, \Delta t/2)\end{array}}{2\Delta y} \\
(\widehat{Q}_{myx})_{P'} &= \frac{\begin{array}{l}Q_{my}(C, 0, 0, \Delta t/2) - Q_{my}(A, 0, 0, \Delta t/2) \\ + Q_{my}(E, 0, 0, \Delta t/2) - Q_{my}(G, 0, 0, \Delta t/2)\end{array}}{2\Delta x}
\end{aligned} \tag{16}$$

Here $(Q_x)^{\pm}_{P'}$ and $(Q_y)^{\pm}_{P'}$ are defined as:

$$\begin{aligned}
(Q_{mx})^-_{P'} &= -\frac{1}{\Delta x}\left[Q_m\left(A, 0, 0, \frac{\Delta t}{2}\right) + Q_m\left(G, 0, 0, \frac{\Delta t}{2}\right) - 2(Q_m)_{P'}\right] \\
(Q_{mx})^+_{P'} &= +\frac{1}{\Delta x}\left[Q_m\left(C, 0, 0, \frac{\Delta t}{2}\right) + Q_m\left(E, 0, 0, \frac{\Delta t}{2}\right) - 2(Q_m)_{P'}\right] \\
(Q_{my})^-_{P'} &= -\frac{1}{\Delta y}\left[Q_m\left(A, 0, 0, \frac{\Delta t}{2}\right) + Q_m\left(C, 0, 0, \frac{\Delta t}{2}\right) - 2(Q_m)_{P'}\right] \\
(Q_{my})^+_{P'} &= +\frac{1}{\Delta y}\left[Q_m\left(E, 0, 0, \frac{\Delta t}{2}\right) + Q_m\left(G, 0, 0, \frac{\Delta t}{2}\right) - 2(Q_m)_{P'}\right]
\end{aligned} \tag{17}$$

The weighted equation is: $W[x_+, x_-, \alpha] = (|x_+|^\alpha x_- + |x_-|^\alpha x_+)/(|x_-|^\alpha + |x_-|^\alpha)$, and α is a constant ($\alpha = 2$ in this study) (Chang, 1995). It should be noted that $(Q_m)_{P'}$ cannot

be obtained explicitly from Eq. (9) due to the source term $(S_m)_{P'}$. As is a function of $(Q_m)_{P'}$, a local Newtonian iterative procedure is usually needed to determine $(Q_m)_{P'}$. In the present work, to avoid the iterative procedure and save computation time, $(S_m)_{P'}$ is replaced by their linear prediction of current time in Eq. (13) (Yang et al., 2009).

$$(Q_m)_{P'} + \frac{1}{24}\frac{\Delta x}{\Delta y}(Q_{mxx})_{P'} + \frac{1}{24}\frac{\Delta y}{\Delta x}(Q_{myy})_{P'} = \frac{1}{4}\left(\bar{Q} + \frac{\Delta t}{\Delta x}\bar{E} + \frac{\Delta t}{\Delta y}\bar{F}\right) + \frac{\Delta t}{8}\bar{S} \qquad (18)$$

$$\tilde{S} = \bar{S} + \frac{\Delta t}{4}\bar{S}_t$$

where $\bar{S}_t$ is the time derivative of $\bar{S}$. $(Q_m)_{P'}$ can be directly solved without any iteration, since the time derivative of $(S_m)_A$, $(S_m)_E$, $(S_m)_C$ and $(S_m)_G$ is all known at current time.

3. Model evaluation

3.1. Water and kerosene interaction in T-shaped tube

Dong et al. (2008) set up an experiment, in which two-phase flow problem in a T-shaped micro-fracture was considered. The width and depth of the T-shaped micro-fracture are 6 mm and 3 mm, respectively. The size of L is 6 mm. For detailed information about the experimental instruments and the experimental process, readers refer to the lecture (Dong et al., 2008). The motion of the mass interface and the mixture as well as separation process are observed by CCD-Scanning system. This process is also numerically simulated by CE/SE scheme coupled with HPLS method, by simplifying the three dimensional (3D) problem into the 2D problem as shown in Fig. 4(a). The mesh grids are 100×200 and the time interval is 0.0005 s. The surface force between the oil, water and solid wall is taken into account. The wall boundary condition is introduced. The left and right boundaries are subject to the inlet condition and the outlet boundary is imposed on the bottom. The contact angle boundary is assigned to the interface between the wall and fluids by level-set function. The parameters used are summarized in Tables 1 and 2. When the fluid has come into becoming stable, the experimental data and CE/SE calculated results are demonstrated in Fig. 4(b) and (c). The interface between water and kerosene is clear. The CE/SE method accurately captures the interface and the separation process. It can be seen that the numerical results by CE/SE scheme coupled with HPLS method match the experimental data well.

Table 1
Property of kerosene and water used in this model.

Fluid	Density (kg/m^3)	Viscosity (Pa s)	Surface force (N m^{-1})
Kerosene	780	0.000115	0.045
Water	998.2	0.001	

Table 2
Calculated parameters for three cases.

Inlet velocity	m/s	Re	We	Case
0.2778^K	-0.2778^W	83.1	0.514	i
0.0185^K	-0.00093^W	5.54	0.00228	ii
0.185^K	-0.00926^W	55.4	0.228	iii

Minus "–" denotes the flow direction. Index of K and W presents kerosene and water, respectively.

3.2. Dam break problem

For further validation of the CE/SE scheme coupled with HPLS method, the dam break problem (Martin and Moyce, 1952) is numerically calculated. A 81×41 uniform Cartesian grid is applied with an initial water column height to width ratio of 2. Densities of water and air are 1000 kg/m^3 and 1 kg/m^3, respectively. Viscosities of water and air are 0.001 kg/(ms) and 0.00001 kg/(ms), respectively. The calculated domain is 0.285 m $\times$ 0.0675 m. The porosity and Darcy number are 0.9 and 10^4, respectively. At the outlet boundary, the Neumann boundary condition is set for velocities. At all other boundaries, slip wall boundary conditions are applied. Fig. 5(a) shows the phase interface profiles between time of 0.0 s and time of 0.24 s with time interval 0.08 s. The water surface evolves in a smooth shape and no oscillation occurs at the interface near the solid wall. Fig. 5(b) depicts the history of the water front marching along the ground surface ($y = 0$). It proves that the numerical results well satisfy with the experimental data.

4. Flow instability in CO_2 storage in saline aquifer

Simulations of immiscible two-phase fluid flow instability were also carried out to test the validity of the proposed model. As a benchmark problem, Taylor instability problem is commonly used to study the effects of fluid density differences (under the influence of gravity) and viscosity ratios on the stability/instability of immiscible flows. In this case, a high density liquid is placed over a low density liquid in a rectangular domain of dimension 1 m $\times$ 4 m with a mesh resolution of 64×256. First we considered the displacement of a less dense fluid by a denser fluid. To initiate the instability at the fluid–fluid interface, the initially flat front was perturbed by a sinu-

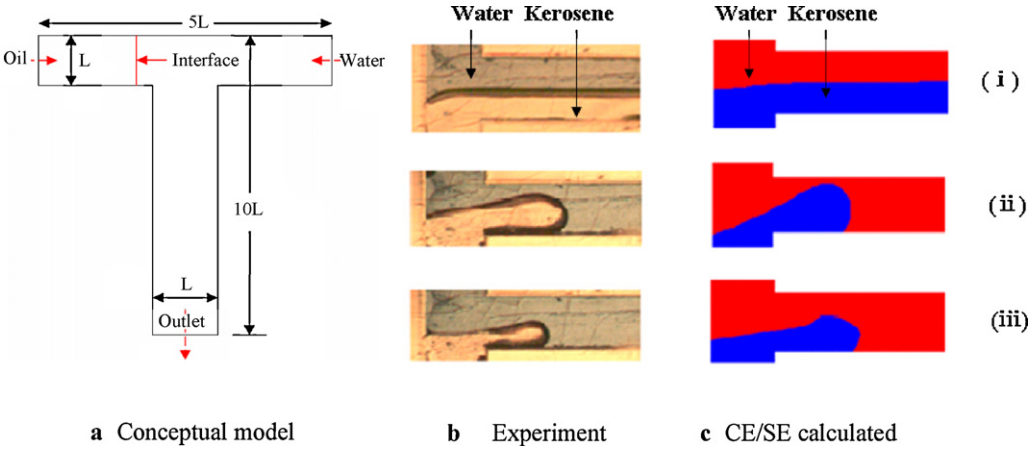

Fig. 4. Concept model and experimental (Dong et al., 2008) and the CE/SE calculated results for Re = 83.1, We = 0.514 (i), Re = 5.54, We = 0.00228 (ii), and Re = 55.4, We = 0.228 (iii), respectively.

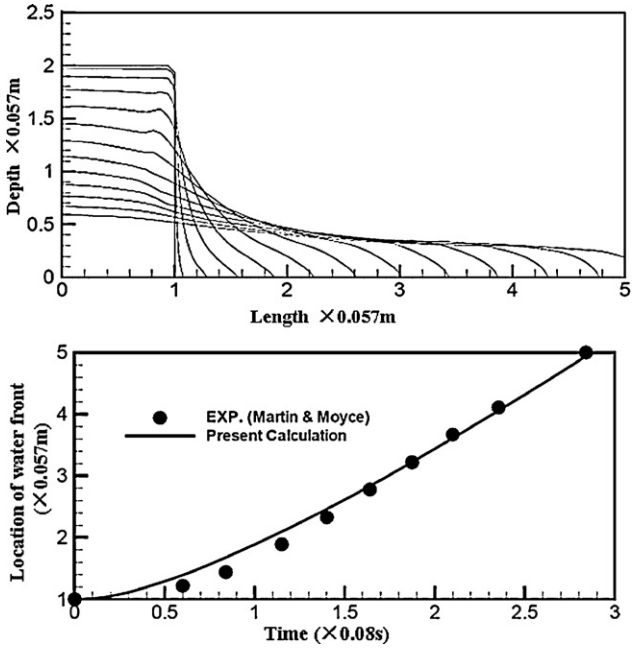

Fig. 5. (a) Evolution of the free interface and (b) history of water front location at $y = 0$ from time = 0.0 to 0.24 s with time interval 0.08 s.

soidal deformation (Guermond and Quartapelle, 2000). The ratio of viscosity and density is 1 and 3, respectively, for Re = 1000. We assume that the porosity and Darcy numbers are 0.9 and 1.0×10^4 (Yang et al., 2009). The slip boundary conditions are applied to the left and right sides, while non-slip boundaries for the top and down sides. Fig. 6 shows that as time increased, the phase or fluid interface varied from a single smooth finger to a highly unstable fragmented dendritic. The results are in excellent agreement with that obtained by Guermond and Quartapelle (2000).

Next, numerical simulations of supercritical flow instabilities in CO_2 storage in saline aquifers are performed. A basic assumption is that CO_2 and salt water do not mix and local thermal equilibrium state is obtained. We assume the saline aquifer is the isotropic and homogeneous porous media. We studied the displacement of more viscous and denser saline water with a less viscous and less denser supercritical CO_2 in a saturated saline aquifer. In a closed box, we start with the unstable equilibrium position, where salt water is on top of supercritical CO_2. The parameters are defined based on the in situ geological data from Jiling oil field (Li, 2009) and the surface tension is based on the experiment (Chiquet et al., 2007). The ratio of viscosity and density is 1.125 and 0.05, respectively. The

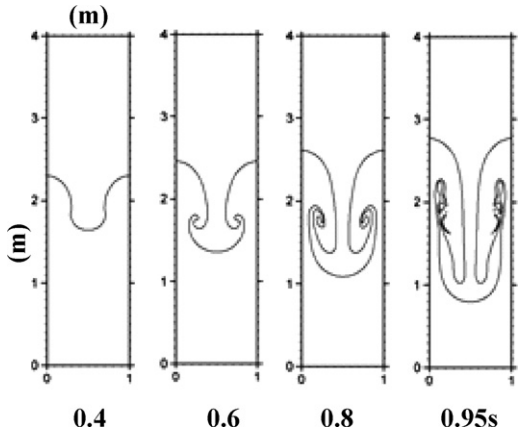

Fig. 6. Finger evolution calculated by CE/SE method after 0.4, 0.6, 0.8 and 0.95 s.

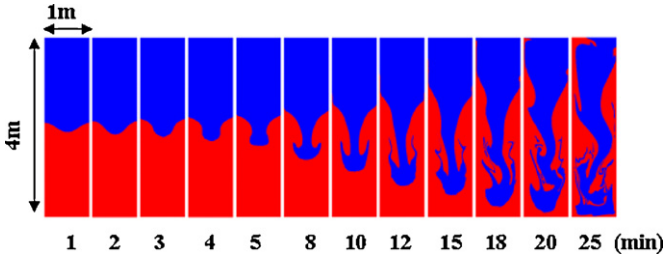

Fig. 7. Finger evolution presenting deformation and motion of the interface for different times. The blue region presents the brine water, while the red one denotes the CO_2. (For interpretation of the references to color in this figure legend, the reader is referred to the web version of this article.).

average porosity and permeability are 0.25 and 1.23×10^{-10} m^2, respectively (Zhang, 2009). The calculation domain is 1 m × 4 m. 100×400 collocated uniform meshes are employed for the computation. As shown in Fig. 7, the onset and propagation of viscous fingers during immiscible displacement of CO_2 by brine water was presented. The displacement was found to be unstable, resulting in formation of fingers. Before time $t = 15$, displacement resulted in the formation of a single smooth finger. As time increased, the finger became unstable. At time of 18, displacement resulted in finger splitting. As time reached to 20, displacement resulted in the formation of a highly unstable fragmented dendritic structure. At time of 25, the flow fully developed to be turbulent. In our simulations, the behavior of the front depended only on the properties of the saline water and CO_2 and direction of the body force (gravitational forces).

5. CO_2 dissolution in saline aquifer

In this section, we consider the mass transport mechanism between CO_2 and saline water in order to assess the multiphase process and interpret the solubility capture of CO_2 geological storage over time up to 300 years and study mechanisms of motion and deformations of fluid interface. We first assume that (1) CO_2 can partially mixes with saline water and the chemical reaction is the first order and not inverse; (2) the mass transfer is assumed to have no impact on the physical properties of the system; (3) the two fluids are viscous, Newtonian, incompressible and isothermal; and (4) the interface tension is taken as constant and there is no interfacial resistance to mass transport. The multi-phase flow in porous medium involves low velocity and dominant effect of surface forces between fluid/fluid and fluid/surface interfaces. The phenomenon can be characterized by the surface tension coefficient which represents the relative effect of viscous forces versus surface tension acting across an interface between two immiscible liquids. Table 3 lists parameters used in the simulations. The 2D model is a homogeneous sandstone formation of 50 m length and of 100 m thickness. 200×400 uniform meshes are used for the computation. The average porosity and permeability of the sandstone formation are 0.20 and 2.65×10^{-15} m^2, respectively. At all boundaries, slip wall boundary conditions are applied for the velocities, while the Neumann boundary condition is set for mass transport.

Table 3
Parameters listed for this simulation.

Density (kg/m^3)	1045 (brine water)	783 (CO_2)
Viscosity (Pa s)	2.535×10^{-4} (brine water)	3.95×10^{-5} (CO_2)
Surface force (mN m^{-1})	23.0	
Diffusivity (m^2/s)	1.0×10^{-9}	
Porosity	0.2	
Permeability (m^2)	2.65×10^{-15}	

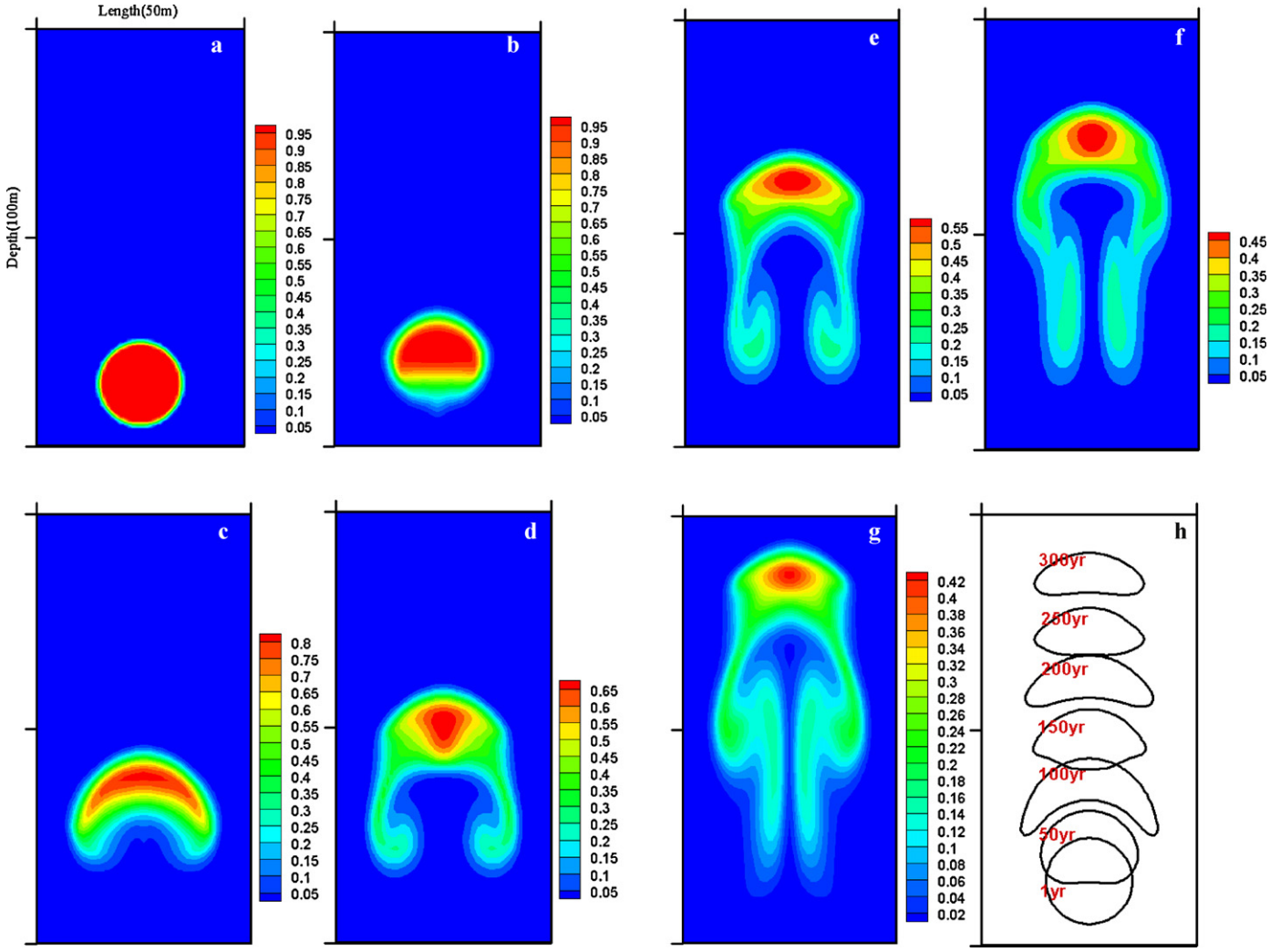

Fig. 8. Predicted solute concentration distribution in both phases and the velocity vector field relative to the drop motion after time of (a) 1 year, (b) 50 years, (c) 100 years, (d) 150 years, (e) 200 years, (f) 250 years and (g) 300 years and (h) evolution of predicted fluid interface.

The quantitative simulation of interphase mass transport is turned out to be especially challenging, due to different diffusivities in two liquid phases and the distribution coefficient of a solute not equal to unity (the latter leads to the solute concentration discontinuous across the interface, and the former results in the discontinuity of concentration gradient). Special care must be taken for resolving these discontinuities in the numerical simulation. In order to keep the concentration continuous at the interface, the variable transformations (Yang and Mao, 2005) are adopted. In practical situations the mass transport to/from a drop occurs normally before the motion of the drop approaches steady state. Performance results have been obtained on the Microsoft Windows PC with dual core. The problem consists of 80,000 blocks with the grid size used of 0.25 m, and total execution CPU time is 15 min.

Fig. 8(a)–(g) illustrates the predicted solute distribution in both phases and the velocity vector field relative to the drop motion at selected times for this case. The results show that the shape of the drop was gradually deformed into a spheroid from its initial spherical shape, and a toroidal recirculation was formed within the drop. The results demonstrate that in the center part of the drop the solute concentration gradually decreased as it was swept by the recirculation towards the drop surface and then towards the rear of the drop, where it entered the continuous phase as a plume, suggesting that convective mass transport did play an important role. The plume was more distinct at early time when the concentration of the drop was highest.

Fig. 8(h) demonstrates the evolution of phase or fluid interface shown as a set of superimposed calculations. As CO_2 droplet is pushed by buoyancy, gravity and surface tension, it starts to move up and deform. Due to the pressure difference between the upper and lower surfaces, the vortex chain at the corner of the upper surface is formed, which induces the jet motion that pushes brine water into CO_2 droplet from down. Effects of the jet result in a velocity difference between the upper and lower surfaces, and so the lower surface approaches the upper surface of CO_2 droplet. Because of the higher pressure difference between the upper and lower surfaces, which drives the lower surface up, CO_2 droplet flattens. Due to the solution process, CO_2 droplet gradually diminishes as time increases.

Fig. 9 depicts the evolution of the averaged concentration of inner CO_2 droplet. As the time increases, the concentration is gradually decreased. At time of 100 years, that concentration reduces by 25%. It indicates that the hydrodynamic trapping dominates the motion and deformation CO_2 droplet, while dissolution process of CO_2 also has a great influence on CO_2 sequestration. It implies that in the short-term period (150 years), lots of CO_2 remain as a free supercritical phase (hydrodynamic trapping), and the amount dissolved in the brine water (solubility trapping) gradu-

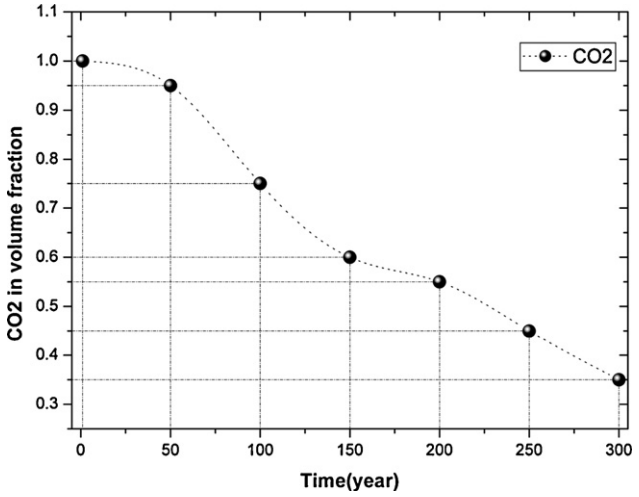

Fig. 9. Evolution of averaged concentrations of inner droplet relative to that of the original droplet.

ally increases. Later, hydrodynamic trapping decreases, solubility trapping increases significantly due to the migration and diffusion of CO_2 plume and the convective process.

It notes that our simulation results are specific to the conditions and parameters considered. The present studies did not take into account of media heterogeneities, anisotropic characteristics and geometric complexities. The "numerical experiments" presented here give a detailed view of the dynamical interplay between hydrodynamic and simple dissolution processes, which could be useful for the fundamental studies on two-phase CO_2–water flow dynamics with possible applications to CO_2 storage in deep saline aquifers. Hydrogeological parameters such as anisotropic permeability could have significant effects on simulation results (Audigane et al., 2007). Especially they can affect the spatial distribution of the injected CO_2 in the formations (Zhang et al., 2009). Parameter sensitivity simulations should be carried out to examine these effects, and also the CO_2 mineral trapping mechanism should be considered in the future. Numerical simulation program should be developed for chemically reactive non-isothermal flows of multiphase fluids in CO_2 storage.

The main advantages of the current CE/SE scheme coupled with HPLS method, referred to as CCS_MULTIF (multiphase flows model for CCS), are that CCS_MULTIF is based on fluid dynamical conservation laws, capturing physics, such as hydrodynamic and solubility trapping, more efficiently and realistically, and can give the high resolution and accuracy on fluid fields and the positions of phase interface between CO_2 and brine water in saline aquifers. CCS_MULTIF source code developed in this study includes the state of equation (EOS) for CO_2 covering the triple point temperature and pressure to the supercritical region. The geological heterogeneity has been implemented, interfacing the well known geostatistical model (GSLIB) (Deutsch and Journel, 1998). CCS_MULTIF should be a new high-resolution and genuinely multidimensional paradigm for solving the process of CO_2 hydrodynamic trapping. The computational scheme developed currently is clear in physical concept, easy to be implemented and high accurate and efficient for the problems considered. Our current method should be straightforward applied to three-dimensional field-scale CO_2 geological storage in deep saline aquifers. CCS_MULTIF is written in both FORTRAN 95 and C++. It has been tested on two computer platforms, including Microsoft Windows and Linux-based PCs. The computer memory required by CCS_MULTIF depends on the problem size such as numbers of grid blocks, hydrological parameters and geological heterogeneities.

6. Conclusion

This paper presents a phase interface mechanism for the stability simulation of the density-driven convection in CO_2 storage in deep saline aquifers. An upgraded CE/SE scheme and hybrid particle level-set method has been applied to model the multi-phase flow through porous medium. The model predictions match well with the experimental measurements of fluid or phase interface. The stability of a density-driven convection in isotropic and homogenous saline aquifers targeted for sequestering CO_2 is investigated with two phase flow simulation. By assuming infinitely small perturbations, the onset and propagation of viscous fingers during immiscible displacement of CO_2 by brine water was performed. As time increases, the displacements lead to the formation of a highly unstable fragmented dendritic structure, and finally the flow fully develops be turbulent. Then, CO_2 dissolution in saline aquifer is investigated. The results show that the shape of the droplet was gradually deformed into a spheroid from its initial spherical shape, and a toroidal recirculation was formed within the droplet. Hydrodynamic trapping dominates the migration and build-up of CO_2 in the saline aquifers, while the convective mass transport also has a great influence on CO_2 sequestration. Based on the physical conservation laws, the proposed CE/SE scheme coupled with HPLS method can capture multiphase fluid physics process, phase interfaces (CO_2/brine water) and stability of phase interfaces more efficiently and realistically. The computational scheme developed currently is clear in physical concept, easy to be implemented and high accurate and efficient, which could be useful for fundamental studies on two-phase CO_2–water flow dynamics with possible applications to CO_2 storage in deep saline aquifers.

Acknowledgments

This work is supported by National '973' project under the grant number (2006CB7058 and 2011CB707303). The first author is partially supported by the European Scientific Foundation (ESF). We are very grateful to two anonymous reviewers and the Associate Editor, Dr Ziqiu Xue for providing many constructive comments and suggestions, which improved this manuscript.

References

Audigane, P., Gaus, I., Czernichowski-Lauriol, I., Pruess, K., Xu, T., 2007. Two-dimensional reactive transport modeling of CO_2 injection in a saline aquifer at the Sleipner site, North Sea. American Journal of Science 307, 974–1008.

Bachu, S., 2000. Sequestration of CO_2 in geological media: criteria and approach for site selection in response to climate change. Energy Conversion and Management 41, 953–970.

Bachu, S., Gunter, W.D., Perkins, E.P., 1994. Aquifer disposal of CO_2: hydrodynamic and mineral trapping. Energy Conversion and Management 35, 269–279.

Brackbill, J.U., Kothe, D.B., Zemach, C., 1992. A continuum method for modelling surface tension. Journal of Computational Physics 100, 335–354.

Caltagirone, J.P., 1980. Stability of a saturated porous layer subject to a sudden rise in surface temperature: comparison between the linear and energy methods. Quarterly Journal of Mechanics and Applied Mathematics 33, 47–58.

Chang, S.C., 1995. The method of space–time conservation element and solution element––a new approach for solving the Navier–Stokes and Euler equations. Journal of computational Physics 119, 295–324.

Chiquet, P., Daridon, J.L., Broseta, D., Thibeau, S., 2007. CO_2/water interfacial tensions under pressure and temperature conditions of CO_2 geological storage. Energy Conversion and Management 48, 736–744.

Deutsch, V., Journel, G., 1998. Geostatistical Software Library and User's Guide, second ed. Oxford university press, Oxford.

Dong, H.F., Zhang, D.L., Zhao, Y.C., 2008. Numerical simulation of immisable two-phase flow in T-shaped micro-tube. Journal of Chemical Engineering 59 (8), 1950–1957 (in Chinese).

Ennis, K.J., Paterson, L., 2003. Role of convective mixing in the longterm storage of carbon dioxide in deep saline formations. In: SPE Annual Technical Conference and Exhibition, SPE 84344, Denver, Colorado.

Enright, D., Fedkiw, R., Ferziger, J., 2002. A hybrid particle level set method for improved interfaces capturing. Journal of Computational Physics 176, 205–227.

Guermond, G.L., Quartapelle, L., 2000. A projection FEM for variable density incompressible flows. Journal of Computational Physics 165, 167–188.

Hitchon, B., Gunter, W.D., Gentzis, T., Bailey, R.T., 1999. Sedimentary basins and greenhouse gases: a serendipitous association. Energy Conversion and Management 40, 825–843.
Jiang, G.S., Peng, D., 2000. Weighted ENO schemes for Hamilton–Jacobi equations. SIAM Journal on Scientific Computing 21, 2126–2143.
John, G., 2004. Geological storage of CO_2: what do we know, where are the gaps and what more needs to be done. Energy 29, 1329–1338.
Kenta, S., Takashi, F., Yuichi, N., et al., 2008. Numerical simulation of supercritical CO_2 injection into subsurface rock masses. Energy Conversion and Management 49, 54–61.
Lapwood, E.R., 1948. Convection of a fluid in a porous medium. Proceedings of the Cambridge Philosophical Society 44, 508–521.
Li, M., 2009. Progress towards demonstration in China. In: EFS-FWF-LFUI Conference on CO_2 Geological Storage: Latest Progress, Obergurgl, Austria, 22–27 November.
Liu, Q.L., Vasilyev, O.V., Brinkman, A., 2007. penalization method for compressible flows in complex geometries. Journal of Computational Physics 227, 946–996.
Martin, J.C., Moyce, W.J., 1952. An experimental study of the collapse of liquid columns on a rigid horizontal plane. Philosophical Transactions of the Royal Society of London Series A—Mathematical Physical and Engineering Sciences 244 (882), 312–324.
Osher, S., Sethian, J.A., 1988. Fronts propagating with curvature-dependent speed: algorithms based on Hamilton–Jacobi formulations. Journal of Computational Physics 79, 12–49.
Soong, Y., Goodman, A.L., McCarthy-Jones, J.R., Baltrus, J.P., 2004. Experimental and simulation studies on mineral trapping of CO_2 with brine. Energy Conversion and Management 45, 1845–1859.
Straughan, B., Walker, D.W., 1996. Anisotropic porous penetrative convection. Proceedings of the Royal Society of London A 452, 97–115.
Sussman, M., Smereka, P., Osher, S., 1994. A level set approach for computing solutions to incompressible two-phase flow. Journal of Computational Physics 114, 146–159.
Wang, J.T., Liu, K.X., Zhang, D.L., 2009. An improved CE/SE scheme for multi-material elastic-plastic flows and its applications. Computers and Fluids 38 (3), 544–551.
Whitaker, S., 1996. The Forchheimer equation: A theoretical development. Transport in Porous Media 25, 27–61.
Xu, X.F., Chen, S.Y., Zhang, D.X., 2006. Convective stability analysis of the long-term storage of carbon dioxide in deep saline aquifers. Advances in Water Resources 29, 397–407.
Yang, C., Mao, Z.S., 2005. Numerical simulation of interphase mass transfer with the level set approach. Chemical Engineering Science 60, 2643–2660.
Yang, D.X., Zhang, D.L., 2010. Simulating multiphase flows in porous media with high order CE/SE method. In: Book of Abstracts of the 5th Conference international Marangoni Association (IMA5): Interfacial Fluid Dynamics and Process, Florence, Italy, 7–10 June, pp. 148–149.
Yang, D.X., Li, G.M., Zhang, D.L., 2009. A CE/SE scheme for flows in porous media and its application. Aerosol and Air Quality Research 9 (2), 266–276.
Yang, D.X., Zhang, D.L., Zeng, R.S., et al., 2010. Calculation of multiphase flows in porous media based on CE/SE method. Chinese Journal of Geophysics 53 (1), 189–196 (in Chinese).
Zhang, W., Liu, Y., Xu, T., et al., 2009. Long-term variations of CO_2 trapped in different mechanisms in deep saline formations: a case study of the Songliao Basin, China. International Journal of Greenhouse Gas Control 3 (2), 161–180.